Arch. Mech., 32, 4, pp. 549–577, Warszawa 1980

Radiation, welding, temperature and strain rate influence on material properties in fast breeder reactors

C. ALBERTINI, M. MONTAGNANI (ISPRA) and R. CENERINI, S. CURIONI (BOLOGNA)

DYNAMIC monoaxial tensile tests were performed to determine stress-strain diagrams for strain rates ranging between 10^{-2} and 10^{3} s^{-1}. Test temperatures were ambient, 400° and 550°C. The techniques used at high strain rate were that of the Hopkinson bar with pre-stressed bar loading device, and a hydropneumatic machine. Low strain rates were obtained with conventional tensile testing machines. Test pieces for the investigation of the effects of welding were manufactured in order to observe the mechanical properties of weld material and of the heat-affected zone. The irradiation was performed in the Rapsodie reactor at Cadarache, up to a fluence of 7×10^{21} n.cm^{-1}, corresponding to a damage of 2.2 dpa, in a sodium environment at a temperature of 400°C. The irradiation was continued in the HFR at Petten, up to a damage of 10 and 30 dpa. The results of these later irradiations are not yet available. Defects due to welding and irradiation accentuated the strain rate sensitivity of the materials remarkably. As far as welding is concerned, it should be noted that: 1) at both room and high temperatures, the high deformation rate induces remarkable instabilities in the flow curves of weld and H.A.Z. materials as compared with the virgin material and with the "static" flow curve of the same material; 2) at high temperature both the weld and H.A.Z. materials show strain rate sensitivities of opposite signs with respect to the virgin material. In fact, it is possible to observe that the strength of the two welded materials decreases and that of the virgin material increases or remains constant as the strain rate increases. Furthermore, the fracture strain of the weld and H.A.Z. materials decreases while that of the virgin material remains constant as strain rate increases. The main effects of irradiation are the substantial increase in the flow stress in tests performed at ambient temperature, at a given strain in the first part of the stress strain diagram and the drastic reduction in ductility with respect to the virgin and thermally aged material. At high temperature the flow stress of the irradiated material tends to decrease slightly with increasing strain rate.

Wykonano próby jednoosiowego rozciągania dla określenia zależności «naprężenie-odkształcenie» przy prędkościach odkształcania zawartych między 10^{-2} i 10^{-3} s^{-1} w temperaturze otoczenia, 400 oraz 550°C. Dla dużych prędkości odkształcenia zastosowano technikę pręta Hopkinsona ze wstępnie naprężonym urządzeniem obciążającym i silnikiem hydropneumatycznym. Dla małych prędkości zastosowano aparaturę konwencjonalną. Próbki do badania efektów spawalniczych wykonano w celu zaobserwowania własności mechanicznych spawu i strefy nagrzanej. Napromieniowania dokonano w reaktorze Rapsodie w Cadarache do wartości dozy $7 \cdot 10^{21}$ n cm^{-1} odpowiadającej uszkodzeniu 2.2 dpa, w atmosferze sodu w temperaturze 400°C. Naświetlanie kontynuowano w HFR w Petten z uszkodzeniami sięgającymi do 10 i 30 dpa. Wyniki tych ostatnich napromieniowań nie są jeszcze osiągalne. Uszkodzenia wynikające ze spawania i napromieniowania zwiększają w sposób istotny wrażliwość materiału na prędkość odkształcenia. Jeśli chodzi o spawanie, to należy podkreślić, że 1) w temperaturach tak pokojowych jak i podwyższonych, duża prędkość odkształcenia wprowadza znaczną niestabilność do krzywych płynięcia materiałów spoiny i strefy nagrzanej w porównaniu z materiałem pierwotnym i «statyczną» krzywą przepływu dla tych materiałów; 2) W wysokiej temperaturze zarówno materiał spoiny jak i strefy nagrzanej wykazuje wrażliwość na prędkość odkształcenia o znaku odwrotnym w stosunku do materiału pierwotnego. Można w istocie zauważyć, że wytrzymałość spawanych materiałów maleje, a materiału pierwotnego wzrasta lub pozostaje niezmieniona przy rosnącej prędkości odkształcania. Ponadto odkształcenie przy pękaniu materiału spoiny i strefy nagrzanej maleje, podczas gdy w materiale pierwotnym pozostaje ono niezmienione przy wzrastającej prędkości odkształcenia. Głównym efektem napromieniowania jest poważny wzrost naprężenia plastycznego w badaniach wykonanych w temperaturze otoczenia (przy danym odkształceniu w pierwszej części wykresu $\sigma - \varepsilon$, jak również drastyczny spadek ciągliwości w stosunku do ma-

teriału pierwotnego i termicznie starzonego. W wysokiej temperaturze naprężenie plastyczne materiału napromieniowanego ma tendencję do słabego obniżania się ze wzrostem prędkości odkształcania.

Проведены попытки одноосевого растяжения для определения завнисимости „напряжение-деформация" при скоростях деформации содержавшихся между 10^{-2} и 10^{-3} сек$^{-1}$, в температуре окружающей среды 400 и 550° С. Для больших скоростей деформации применена техника стержня Гопкинсона с предварительно напряженным нагружающим устройством и с гидропневматическим двигателем. Для малых скоростей применена конвенциональная аппаратура. Образцы для исследования эффектов сварки изготовлены с целью наблюдения менанических свойств шва и нагретой зоны. Облучения проведены в реакторе Рапсоди в Кадараш до значения дозы $7 \cdot 10^{21}$ псм$^{-2}$, отвечающей повреждению 2,2 g/at в атмосфере натрия в температуре 400°С. Облучения продолжались в Петтен с повреждениями, достигающими 10 и 30 g/at. Результаты этих последних облучений еще неизвестны. Повреждения, вытекающие из сварки и облучения, увеличивают существенным образом чувствительность материала на скорость деформации. Если идет речь о сварке, то следует подчеркнуть, что а) так в комнатных, как и повышенных температурах большая скорость деформации вводит значительную нестабильность в кривые течения материалов шва и нагретой зоны по сравнению с первичным материалом и „статической" кривой течения для этих материалов, б) в высокой температуре так материал шва, как и нагретой зоны показывает чувствительность на скорость деформации обратного знака чем первичный материал. Можно в сущности заметить, что прочность материалов подвергнутых сварке уменьшается, а прочность первичного материала возрастает или остается неизменной при возрастающей скорости деформации. Кроме этого деформация при разрушении материала шва и нагретой зоны уменьшается, в то время как в первичном материале остается она неизменной при возрастающей скорости деформации. Главным эффектом облучения является значительный рост пластического напряжения в исследованиях проведенных в температуре окружающей среды (при данной деформации в первой части диаграммы $\delta - \varepsilon$), как тоже решительное падение тягучести по отношению к первичному материалу и к материалу подвергнутому термическому старению. В высокой температуре пластическое напряжение облученного материала стремится к слабому снижению при росте скорости деформации.

1. Introduction

THE DESIGN of nuclear structures subjected to dynamic loading demands special techniques which do not correspond to well-known techniques for static calculations.

In fact the propagation of waves may induce such phenomena as reflection of waves, with concentration of stress and energy in particular points of the structure.

The designer has a difficult task to harmonize the various reactor structures for static and dynamic (accident) conditions of loading. The values of material strength the designer normally uses are those obtained in statics. The tests that we and other researchers have performed on stainless steels at a high rate of strain have shown a stress-strain diagram different from the static diagram.

As far as welded and irradiated materials at different temperatures are concerned, the strain rate has been found to have a strong influence on elongation to rupture and flow stress.

The dynamic tests performed at our laboratory concerned until now stainless steel materials.

Because of the fact that different safety containment structures in nuclear power plants are built up with concrete, we planned to perform dynamic tests also on such a material whose dynamic constitutive equations are poorly known. The properties of concrete

(nonhomogeneity, anisotropy, etc.) render dynamic tests much more complicated than tests on steels.

A special two-dimension dynamic machine was designed at I.R.C. Euratom Ispra for these tests.

In order to find out the strain rate range at which the materials have to be tested, a preliminary analysis of possible accidents in nuclear power plants was performed.

In order to maintain structural integrity during possible accidents, Nuclear Power Plant containment barriers have to be properly designed to resist several impact and over-pressure loadings.

Explosion (as due to sabotage) and core accidents may cause high pressure waves against the barriers.

Special care must be devoted to the design of the reactor pressure vessel by hydrodynamic (for the propagation of pressure pulses on the reactor core) and finite element structural code calculations for the dynamic response.

The analysis of the response of the reactor vessel to a HCDA can be performed by studying separately the propagation of the pressure pulse inside the reactor core and the structural behaviour of the vessel wave.

Explosives may cause strong pressure waves against barriers. For example, 1 Kg TNT gives at a 1 m distance a peak pressure of $2 \cdot 10^6$ N/m^2 with a time duration of the pulse of $3 \cdot 10^{-2}$ s and an impulse (pressure-time integral) of $2.5 \cdot 10^2$ Ns m^2.

Internal and external missiles, aircrafts and drops of heavy structures are the main causes of impact and penetration loadings.

The missiles are usually divided into two categories according to their rigidity:

deformable missiles (such as aircrafts) where the plastic tearing is important;

rigid missiles (such as aircraft engines, valves, parts of turbine, etc.) where the geometry is simpler and can be solved easier.

Two modes of structural damage due to a missile impact have to be considered.

The perforation mode where the missile perforates the structural component. In this case the impacting time is short as compared to the fundamental eigenfrequency of the structure, and the local region impacted by the missile can be isolated from the remaining part of the structure.

The collapse mode where the structural component loses all of its integrity. This problem is solved by a modal analysis of the overall structure.

Various empirical formulas exist for penetration and perforation thickness on concrete, like the Petry formula, the Ballistic Research Laboratory formula, the Army Corps of Engineers formula. Usually these formulas are based on experiments performed with high velocity and small diameter projectiles, while in nuclear plants safety, often low velocity and large diameter missiles must be considered. For example, engines of typical large jet aircrafts weigh $2 \div 3$ tons with diameters of the order of $1 \div 1.5$ m and a velocity of the order of 100 m/s. Use of the aforesaid formulas to such missiles gives unrealistic values for penetration and perforation depths in concrete.

An analytical model was presented [1] for the evaluation of local effects (penetration and scabbing) on a reinforced concrete barrier due to deformable tornado-generated

missiles. Such missiles may have a weight of the order of $100 \div 300$ Kg with velocity ranging from 50 to 150 m/s.

As far as large deformable missiles are concerned, some typical jet aircrafts like Boeing 707–320 and 720 are often considered with their fuselage buckling load. With such loadings the overall stability of the structure is the main problem to be solved.

2. Experimental techniques

2.1. Split Hopkinson bar

The specimen is inserted between two long pressure bars which remain elastic during the impact.

The applied loading and deformation of the specimen are determined from the displacements and forces at the two faces of the pressure bars.

These may be determined from the strain-time histories in the two elastic pressure bars by means of resistance strain-gauge measurements. These separate strain pulses are recorded: the incident loading pulse ε_I, the reflected pulse ε_R (from the incident pressure bar specimen interface) and the transmitted pulse ε_T (from the transmitted pressure bar).

If l_0 and A_0 are the initial length and cross-sectional area of the specimen, respectively, the average strain (ε_S), stress (σ_S) and strain-rate ($\dot{\varepsilon}_S$) in the specimen are given by

$$\varepsilon_S = \frac{2C_b}{l_0} \int \varepsilon_R dt,$$

$$\sigma_S = E\left(\frac{A}{A_0}\right)\varepsilon_T, \tag{2.1}$$

$$\dot{\varepsilon}_S = \frac{2C_b}{l_0}\varepsilon_R,$$

where E — Young's modulus, C_b — wave velocity in the bars, A — cross-sectional area of the pressure bars.

These formulas are valid when:

pressure pulse duration is long in comparison with wave transit-time through the specimen (i.e. when specimen length is small);

stress wave is plain and radial and axial inertia in the specimen can be neglected;

the friction effects in the specimen are negligible.

As far as pressure pulse duration in comparison with wave transit time is concerned, one must consider that the number N of reflections occurring in a specimen of length l_0 is:

$$N = \frac{C_0 \varepsilon_S}{l_0 \dot{\varepsilon}_S}, \tag{2.2}$$

where C_0 is the plastic wave velocity in the specimen.

In order to use the simplified Hopkinson bar formulas, N must be

$$N \approx 10$$

and, according to formula (2.2), as strain-rate increases the specimen length l_0 must correspondingly decrease.

The aforementioned simplified approach can be used as a guide and each particular situation must be analyzed in detail.

2.2. Corrections on split Hopkinson bar theory

The effects of inertia are summarized in Fig. 1 [2] where the results calculated by a numerical code are compared to Davies and Hunter's approximate correction for axial and radial inertia:

$$\frac{\sigma_S-\sigma_b}{\sigma_b} = \frac{\frac{d^2\varepsilon_S}{dt^2}\varrho_0 d_0^2}{\sigma_b \cdot 6}\left[\left(\frac{l_0}{d_0}\right)^2 - \frac{3}{4}\nu_0^2\right], \tag{2.3}$$

where σ_b is the average axial stress in the two bars, ν_0, ϱ_0, d_0 are the Poisson ratio, density and, diameter, respectively, of the specimen.

As far as the Poisson ratio is concerned, it is a parameter influenced by strain-rate; dynamic values can be measured by a capacitance gauge mounted on the specimen [3].

The numerical results have been obtained by Toody in the form of a two-dimensional elastic-plastic wave propagation computer code.

For the specific configurations considered in Fig. 1, the approximations of Davies and Hunter result in a reasonable correction for inertia effects.

The effects of radial friction is a nonuniform axial stress distribution. RAND [4] presented an analysis based on static Coulomb friction giving an apparent axial stress σ_a:

$$\sigma_a = 2\sigma_S \alpha^{-2}(e^{\alpha}-\alpha-1), \tag{2.4}$$

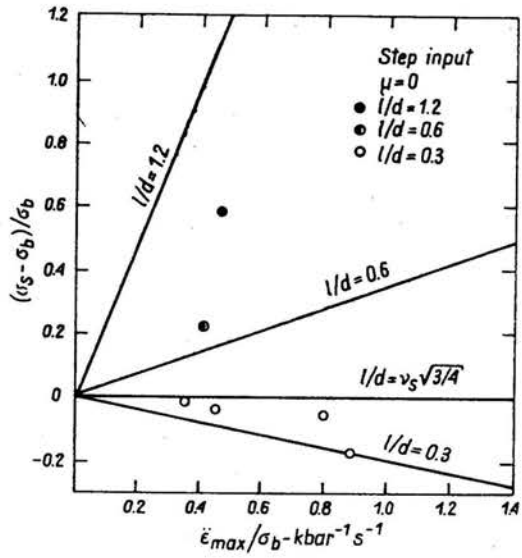

FIG. 1. Comparison of the magnitude of the approximate inertia correction to the calculated errors due to inertia.

where

$$\alpha = \frac{\mu d_0}{l_0}(1+\varepsilon_S)^{-3/2},$$

μ — static Coulomb friction.

Figure 2 compares the numerical results on friction effects obtained by the Toody program with the formula (2.4).

A very important effect of friction can be seen in the non-uniformity of the stress and the strain throughout the sample and the degree of multidimensionality in the stress state.

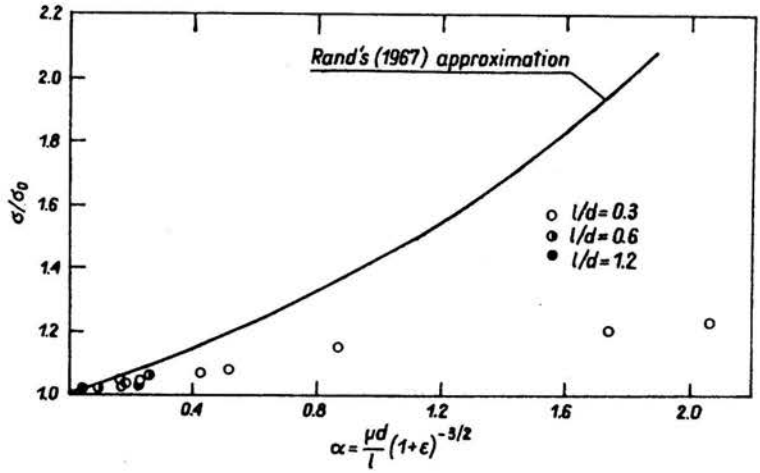

FIG. 2. Comparison of calculated and approximate corrections for friction effects.

Even a friction coefficient of 0.05 can produce a ten-percent variation in axial stress as well as a ten-percent deviation from a one-dimensional stress state [2].

The friction produces an error when the reconstructed stress-strain curve is compared to the input stress-strain curve.

This error could be considered as a strain-rate effect in an experiment if one compares a single dynamic stress-strain curve to a stress-strain curve obtained under quasi-static one-dimensional stress conditions.

A series of code calculations [2] have been performed in order to assess if this error is dependent on strain-rate. Figure 3 compares the reconstructed stress-strain curves for strain rates of 400, 800, 1600, 3300 s^{-1}, for a friction coefficient of 0.05 with results for strain rates of 400 s^{-1} and zero friction. One can see that the error due to the friction coefficient of 0.05 is independent of strain-rate.

Therefore a reasonably small friction coefficient alone does not produce an apparent strain-rate effect. However, one must be certain that equivalent friction conditions are attained in quasi-static tests when results from such studies are compared to results of Hopkinson bar experiments.

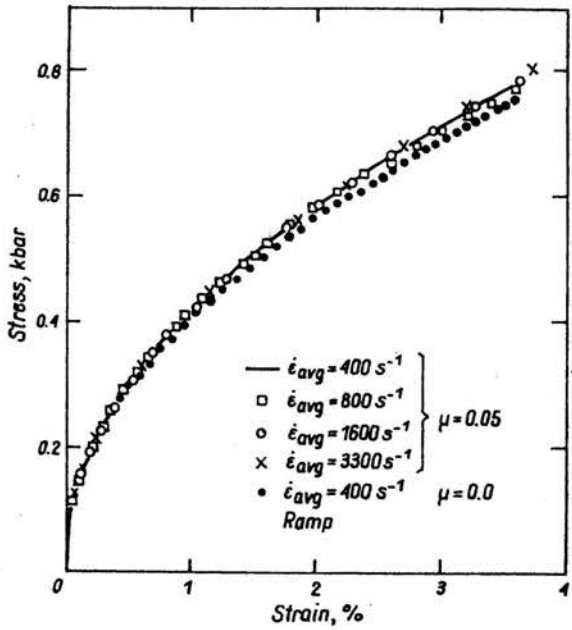

FIG. 3. Indication of the friction-induced material strain-rate effect. No rate-effect present when comparing many rates for the same interface conditions.

3. Experimental results on radiation, welding, temperature and strain-rate influence on stainless steel properties

Dynamic monoaxial tensile tests were performed on some austenitic stainless steels to determine stress-strain diagrams for strain rates ranging between 10^{-2} and 10^{3} s^{-1}. Test temperatures were ambient, 400° and 550°C.

The techniques used at high strain rate were those of the Hopkinson bar with a prestressed bar loading device, and a hydropneumatic machine. Low strain rates were obtained with an Instron machine and a Hounsfield tensometer.

Test pieces for the investigation of the effects of welding were manufactured in order to observe the mechanical properties of weld material and of the heat-affected zone. The irradiation was performed in the Rapsodie reactor at Cadarache, up to a fluence of $7 \times \times 10^{21}$ n. cm^{-2}, corresponding to a damage of 2.2 dpa, in a sodium environment at a temperature of 400°C. The irradiation was continued in the HFR at Petten, up to a damage of 10 and 30 dpa. The results of these later irradiations are not yet available.

The effects of strain-rate on virgin, welded and irradiated materials (up to a damage of 2.2 dpa) are indicated in Figs. 4 to 13.

Defects due to welding and irradiation accentuated the strain rate sensitivity of the material remarkably.

As far as welding is concerned, it should be noted that:

A tboth room and high temperatures, the high deformation rate induces remarkable

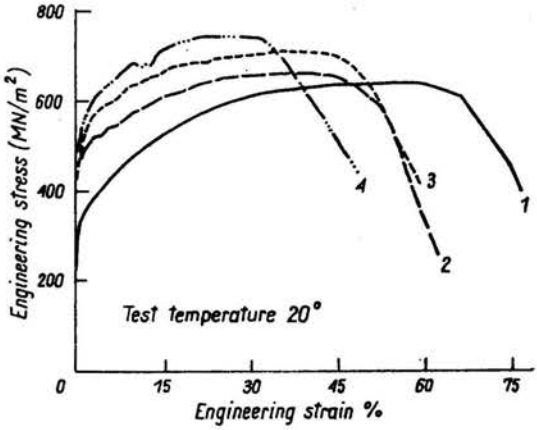

FIG. 4. Stress-strain curves for AISI 316 L stainless steel, virgin. Collaboration Euratom–C.N.E.N. Curve strain-rate; *1* — 0.4×10^{-2} s^{-1}, *2* — 15 s^{-1}, *3* — 44 s^{-1}, *4* — 420 s^{-1}.

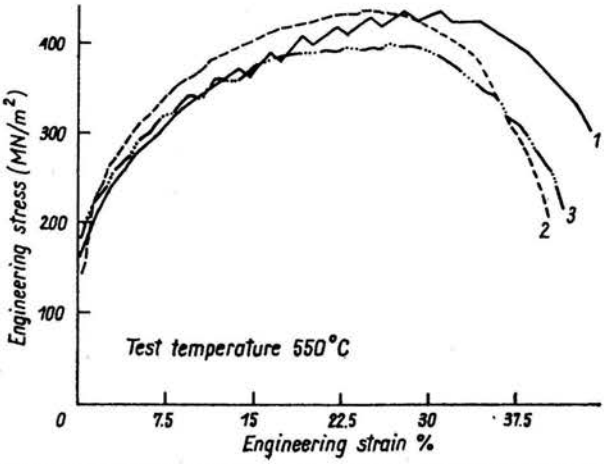

FIG. 5. Stress-strain curves for AISI 316L stainless steel, virgin. Collaboration Euratom–C.N.E.N. Curve strain-rate; *1* — 0.35×10^{-2} s^{-1}, *2* — 8 s^{-1}, *3* — 405 s^{-1}.

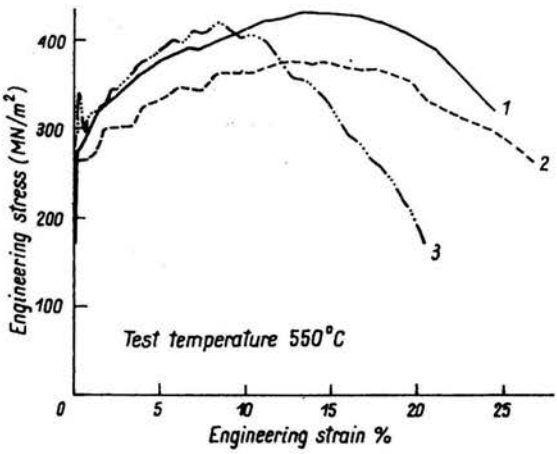

FIG. 6. Stress-strain curves for AISI 316L S.S. weld. Collaboration Euratom–C.N.E.N. Curve strain-rate; *1* — 0.33×10^{-2} s^{-1}, *2* — 40 s^{-1}, *3* — 560 s^{-1}.

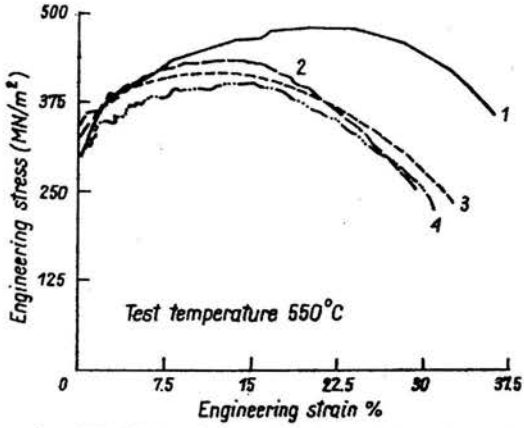

FIG. 7. Stress-strain curves for AISI 316L stainless steel irradiated to 2.2 DPA. Collaboration Euratom-CEA. Curve strain-rate; *1* — 0.35×10^{-2} s^{-1}, *2* — 6.5 s^{-1}, *3* — 39.3 s^{-1}, *4* — 57.2 s^{-1}.

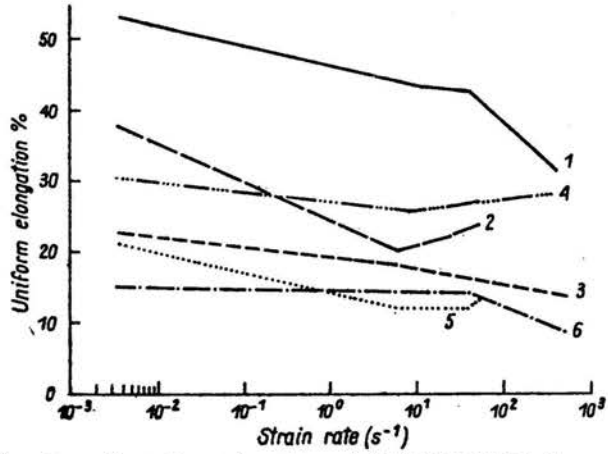

FIG. 8. Effect of strain-rate on the uniform elongation of AISI 316L S.S. Virgin, weld, irradiated to 2.2 DPA at 400°C. Collaboration Euratom-CEA, Euratom-C.N.E.N. *1* — 316L Virgin tested 20°C, *2* — 316L irradiated tested 20°C, *3* — 316L Weld tested 20°C, *4* — 316L Virgin tested 550°C, *5* — 316L irradiated tested 550°C, *6* — 316L Weld tested 550°C.

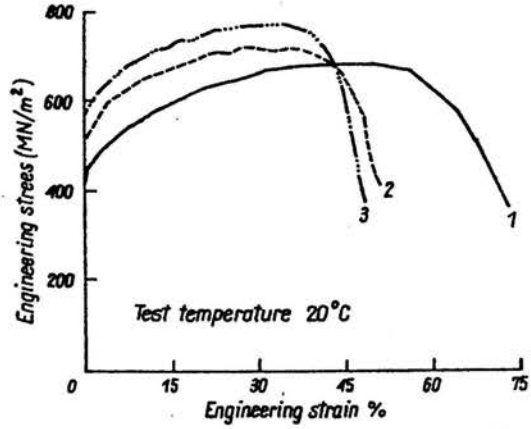

FIG. 9. Stress-strain curves for AISI 304L virgin. Collaboration Euratom-CEA. Curve strain-rate; *1* — 0.38×10^{-2} s^{-1}, *2* — 50 s^{-1}, *3* — 450 s^{-1}.

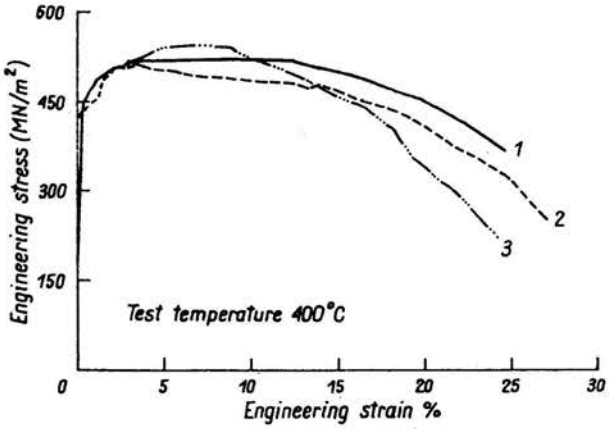

FIG. 10. Stress-strain curves for AISI 304L virgin, collaboration Euratom-CEA. Curve strain-rate; *1*— 0.35×10^{-2} s^{-1}, *2* — 50 s^{-1}, *3* — 500 s^{-1}.

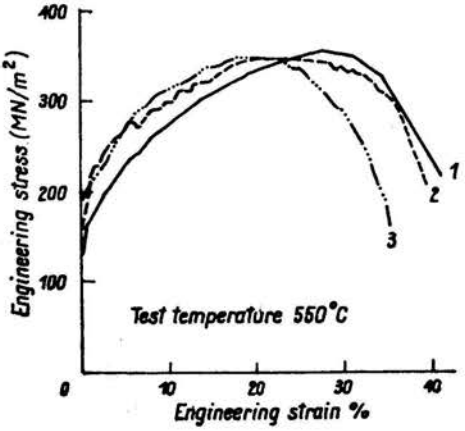

FIG. 11. Stress-strain curves for AISI 304L stainless steel weld. Collaboration Euratom-C.N.E.N. Curve strain-rate; *1* — $0.35 \times 10^{-2} s^{-1}$, *2* — 50 s^{-1}, *3* — 400 s^{-1}.

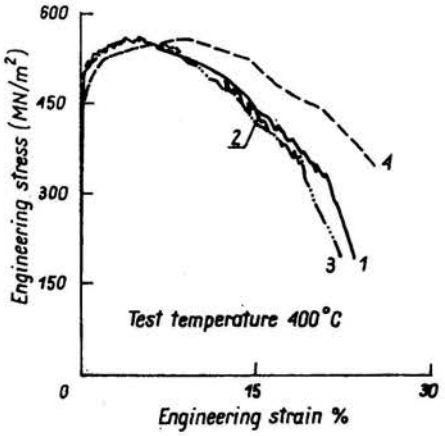

FIG. 12. Stress-strain curves for AISI 304L S.S. irradiated to 2.2 DPA. Collaboration Euratom CEA. Curve strain-rate; *1* — 50 s^{-1}, *2* — 5 s^{-1}, *3* — 23 s^{-1}, *4* — 0.36×10^{-2} s^{-1}.

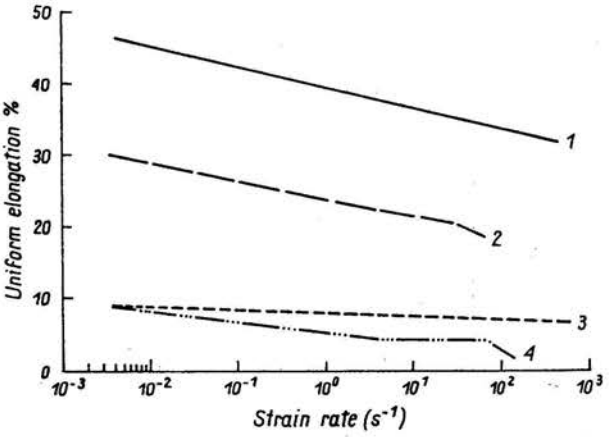

FIG. 13. Effect of strain rate on the uniform elongation of AISI 304L S.S. Virgin and irradiated to 2.2DPA at 400°C. Collaboration Euratom-CEA; *1* — 304L Virgin 20°C, *2* — 304L irrad. 20°C, *3* — 304L Virgin 400°C, *4* — 304L irrad. 400°C.

instabilities in the flow curves of weld and H.A.Z. material as compared with the virgin material and with the "static" flow curve of the same materials.

At high temperature both the weld and H.A.Z. materials show strain rate sensitivities of opposite sign with respect to the virgin material. In fact, it is possible to observe, that the strength of the two welded materials decreases and that of the virgin material increases or remains constant as the strain rate increases. Furthermore, the fracture strain of the weld and H.A.Z. materials decreases while that of the virgin material remains constant as strain rate increases.

The main effects of irradiation are the substantial increase in the flow stress in tests performed at ambient temperature, at a given strain in the first part of the stress-strain diagram and the drastic reduction in ductility with respect to the virgin and thermally-aged material. At high temperature the flow stress of the irradiated material tends to decrease slightly with increasing strain rate.

For example, the superposition of the effects of strain rate and irradiation reduces the uniform deformation at ambient temperature from 52% in the virgin AISI 316L tested under static conditions to 20% in irradiated AISI 316L tested at 60 s^{-1}. At 550°C in the same range of strain rate and for the same materials, the uniform elongation is reduced from 33% to 12.5%.

Experimental values show that there is a considerable influence of strain rate, welding and radiation on stainless steel properties.

The response of a reactor vessel to dynamic loading and the determination of the maximum admissible deformation must take into account the superposition of these effects on the mechanical behaviour of the material.

Furthermore one must consider that in real cases the state of stress on containment structures is multiaxial. In order to find out multiaxial dynamic constitutive equations of the materials (like stainless steel and concrete) of containment structures in a nuclear plant, we plan to perform in the future a set of experiments using some biaxial testing machine.

4. Biaxial testing machines

Existing biaxial testing machines for dynamic loading are described in [5, 6].

They are both biaxial tension-torsion testing machines. In the machine described in [5] the striker bar is made of carbon steel, while the output bar is a copper tube. Different ratios of torque to axial forces are obtained by a suitable clamp mechanism. Wire strain gauges are mounted also on the specimen in a direction parallel to the axis and in a direction inclined to the axis at 45°. The tests were performed with strain rates up to 30—50 s^{-1}.

The machine described in [6] has a pneumatically driven piston which loads the specimen in combined tension and torsion. The machine has the load and displacement capacity to deform plastically all engineering materials over a wide range in deformation rates.

At J.R.C. Euratom Ispra the biaxial dynamic machines for tension and compression loadings have been developed. For the strain rate range $10^{-4}\ s^{-1} \div 10^{-1}\ s^{-1}$ the existing

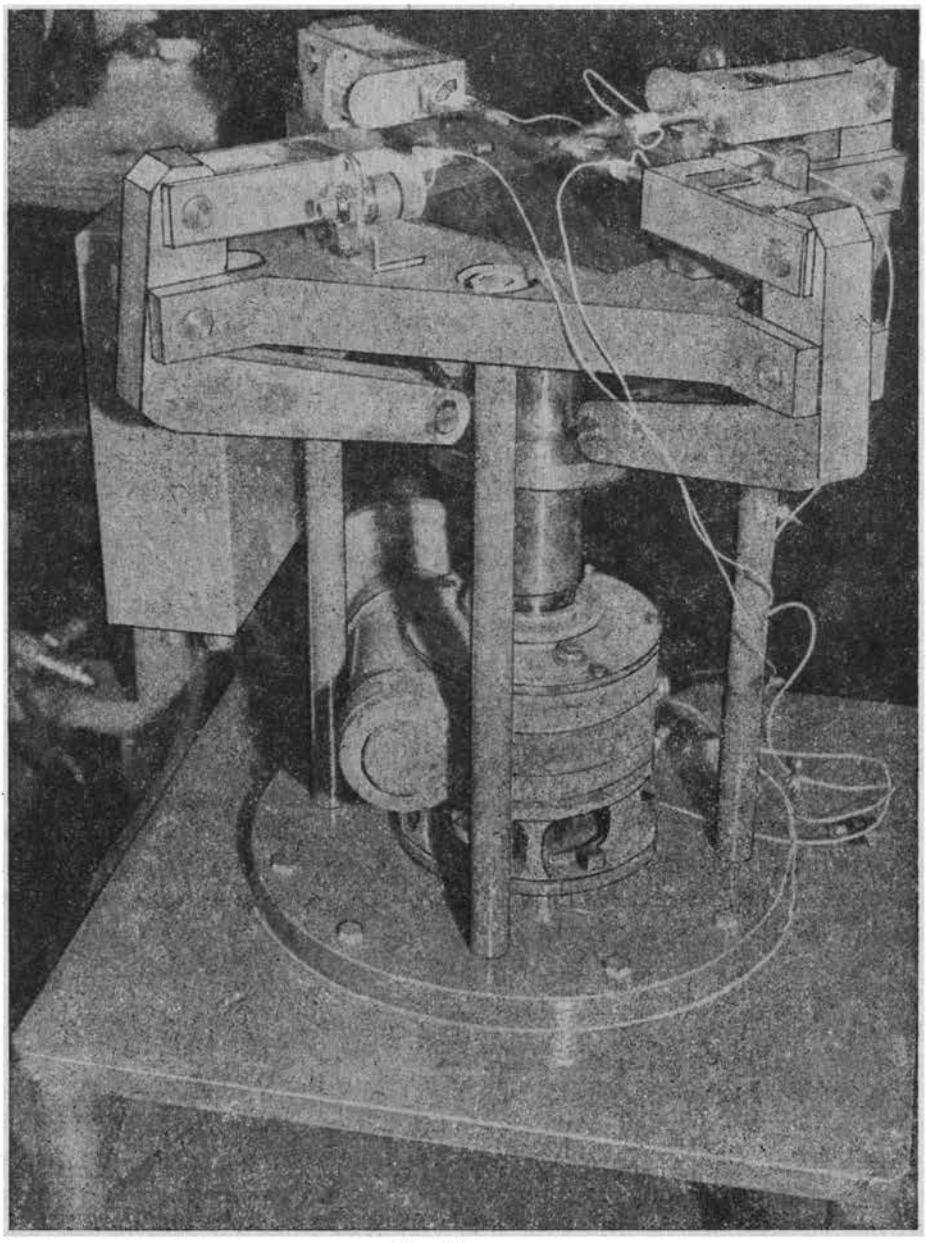

FIG. 14.

device (Fig. 14) has an electric motor which moves a plate pushing simultaneously on four equal arms connected to the specimen. Preliminary tests on stainless steel specimens are being performed where the load sustained by the specimen is measured by strain gauges attached to the four elastic bars.

For the strain rate range $10^{-1}\ s^{-1} \div 10^{-2}\ s^{-1}$ a biaxial testing device (Fig. 15) is under

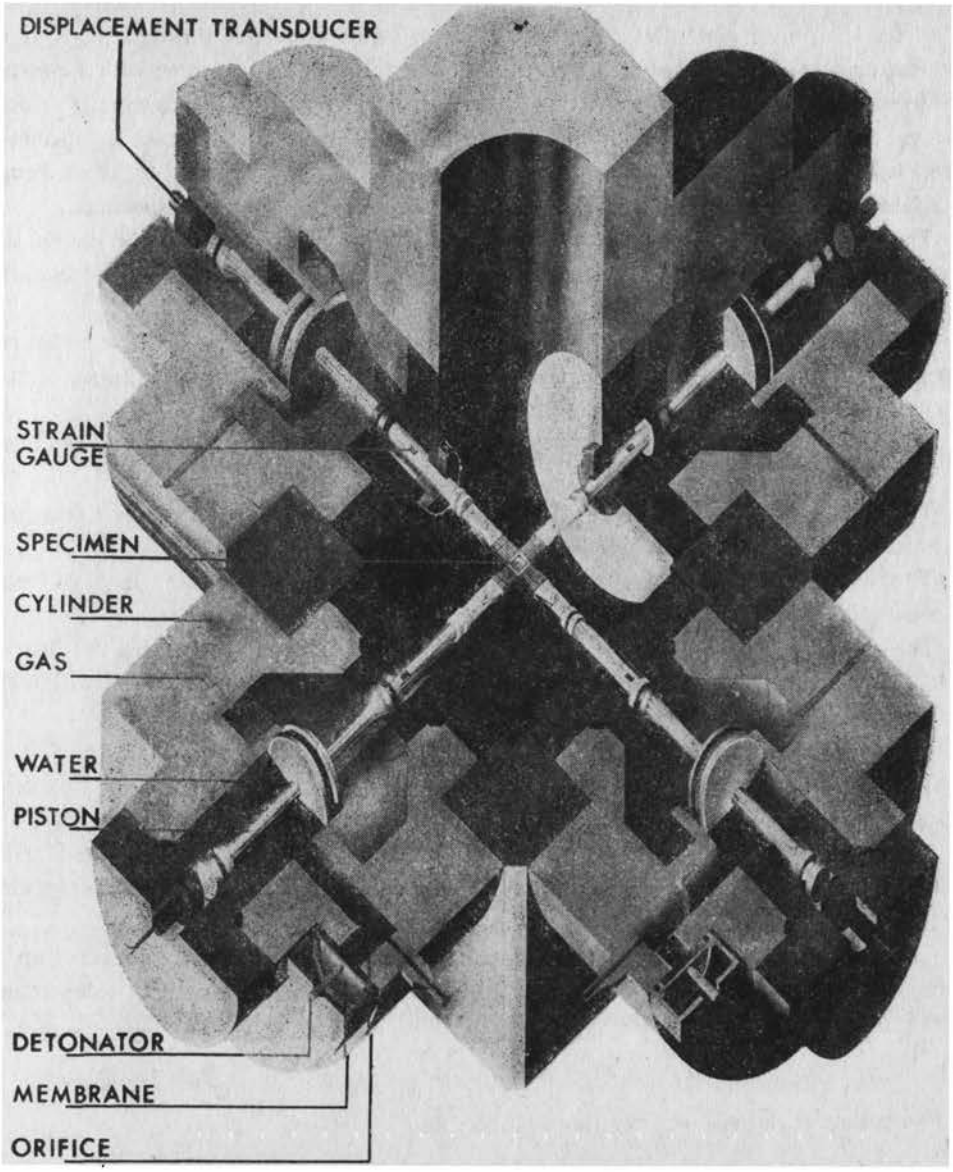

FIG. 15. Biaxial dynamic tensile testing machine Eur. Pat. 1/1808 Lx.

construction consisting of four hydropneumatic elements aligned two by two along two axes at 90°.

The main components of each element are the cylinder, the piston, the gas and water chambers, the discharge orifice and the membrane.

After having loaded both the gas and water chambers at equal pressure, four membranes are broken simultaneously by firing four exploding wire detonators having an operation time of 2 microseconds, thus obtaining the synchronous action of the four pistons connected to the cruciform specimen.

After the four membranes have been broken, water flows out through the four calibrated orifices at a constant rate, thus imposing a strain on the specimen with a constant strain rate. In fact, the pressure acting on the pistons governs the displacement velocity because the load resulting from it is much larger than the force needed to break the specimen. The load sustained by the specimen along the two directions is measured by strain gauges attached to the elastic piston's bars. Strains are measured directly on the specimen.

The action of the pistons can be set up in tension or compression by a simple 180° rotation of the cylinders. Strain rate can be independently controlled along the two axes by changing the diameter of the orifices.

With this machine tests can also be carried out at a constant stress, where strain rate changes rapidly. In this case the water chambers are provided with much larger orifices, thus allowing the pressure above the pistons to drop very rapidly.

Another apparatus for measuring the effect the strain rate effects on large specimens also of concrete is under construction at J.R.C. Euratom Ispra.

The apparatus (Fig. 16) consists of four loading arms at 90°; in the center a cruciform test-piece can be tested along two axes.

The dynamic load is transmitted to the test-piece by four steel tension bars, of length of about 100 m and diameter Ø 70 mm.

These bars, pre-tensioned up to the elastic limit, are able, once broken the fixation bolts, to transmit to the concrete specimen a pressure pulse of 40 ms duration with a rise time of about 200μs, giving a maximum load to the specimen of about 500 tons.

Each bar is loaded by a hydraulic piston.

The tension pulse may be transferred to the specimen as a compression load by using special intermediate pieces.

Strain parameters may also be measured by a fast camera which is able to film the specimen during deformation, recording some marks printed on the surface of the specimen itself.

The device allows to perform tests on relatively large dimensions test-pieces, up to a maximum load of 500 tons, with strain rates between $10^{-4}\ s^{-1}$ and $10^{3} s^{-1}$, depending, among other parameters, on the specimen size.

5. Evaluation on missile concrete impact

As an example of missile concrete impact, we performed Astarte calculations using for the concrete the following constitutive equation:

$$p = a_1\mu + a_2\mu|\mu| + E(b_0 + b_1\mu),$$

where $\mu = \frac{V_0}{V} - 1$, E — Young's modulus, a_1, a_2, b_0, b_2 are material constants, V_0, V — specific volumes (initial and at time t). Concrete and missile are supposed to support also shear stress.

In calculation no 1, the concrete area impacted by missile is supposed to have a velocity of 120 m/s. Figure 17 shows the calculation network before deformation. Figure 18 shows

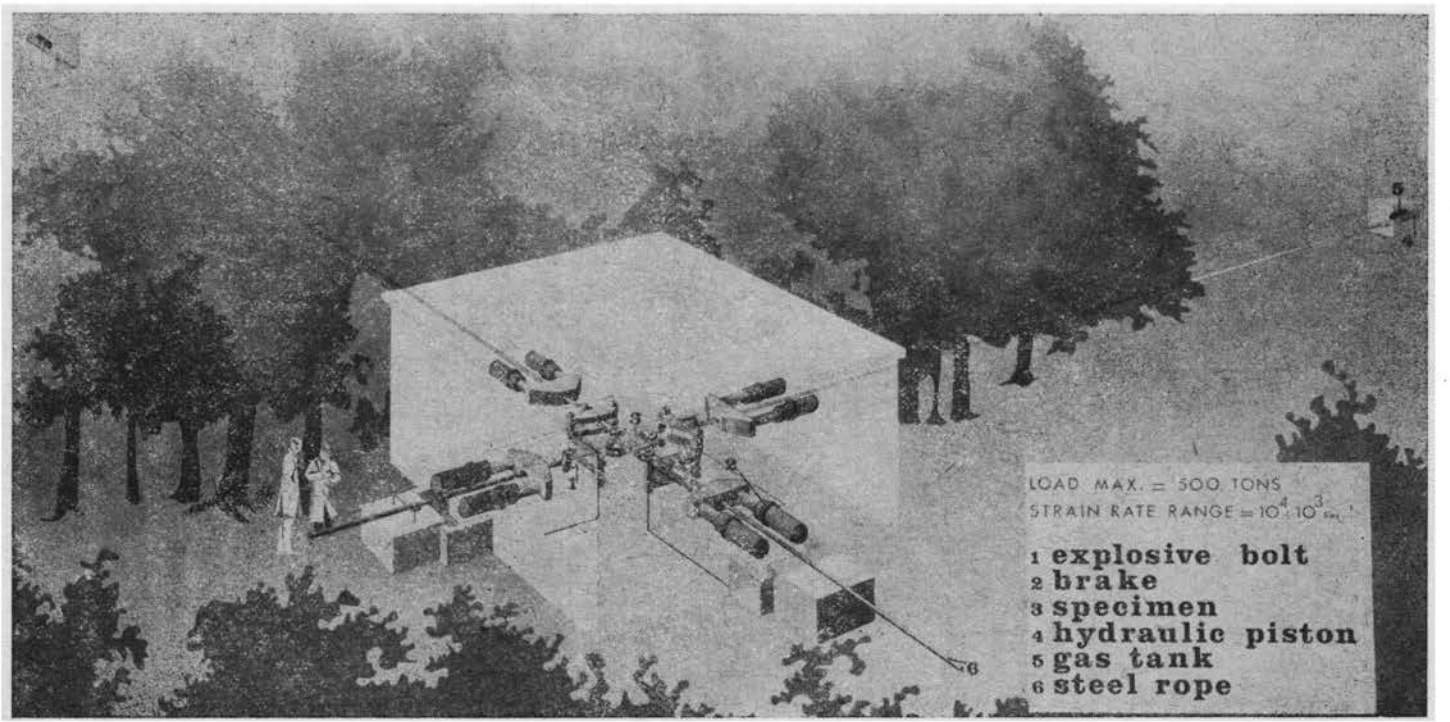

FIG. 16.

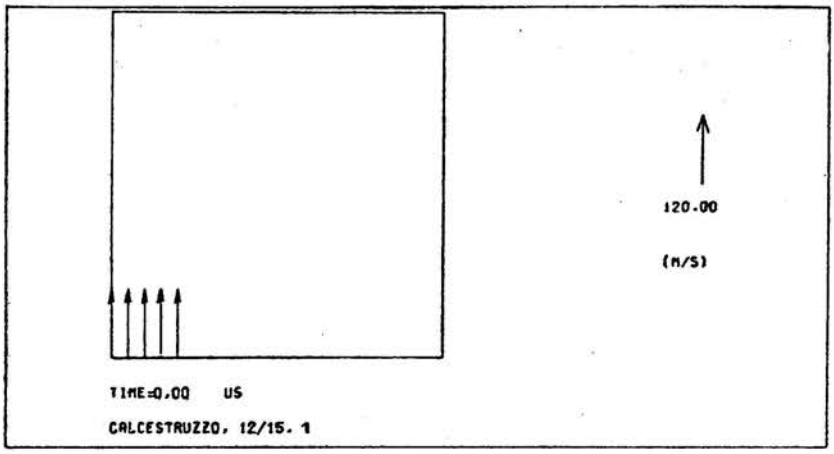

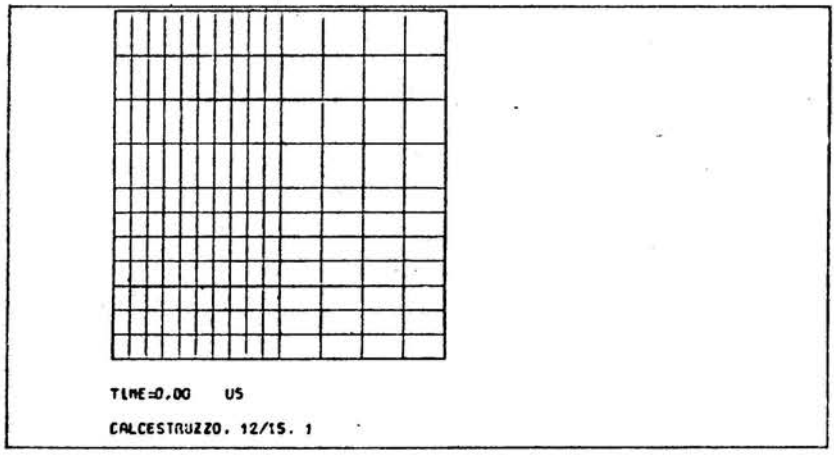

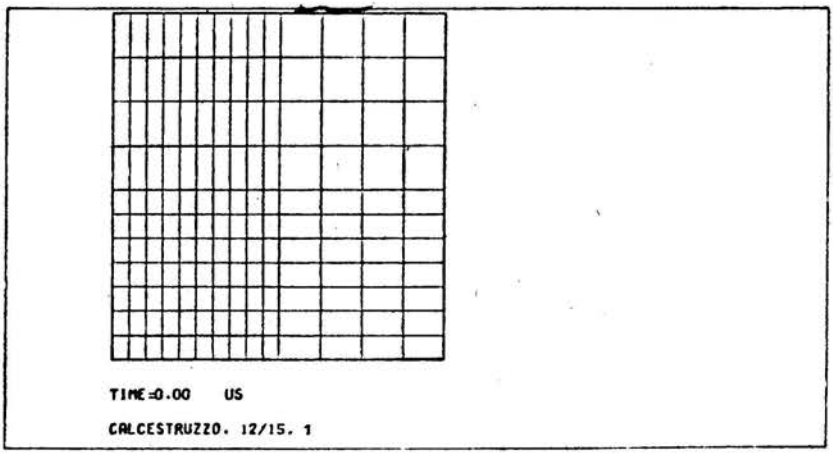

FIG. 17.

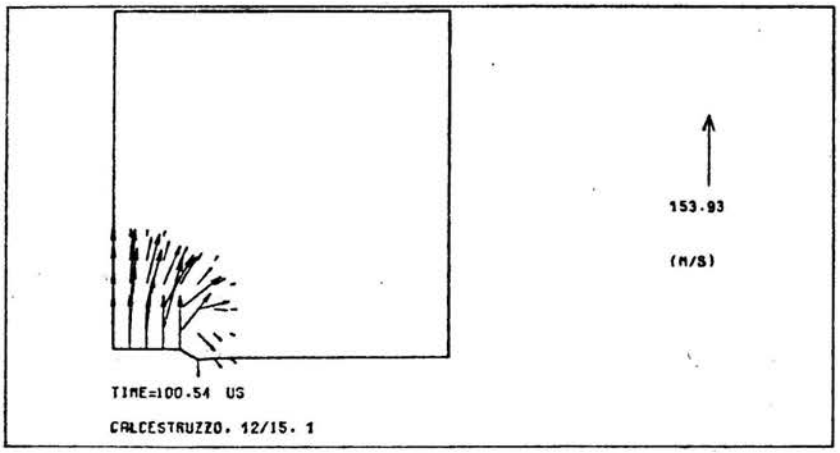

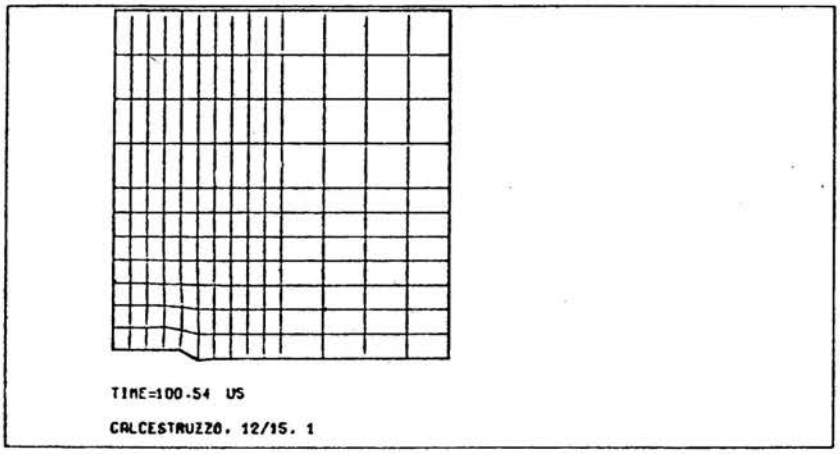

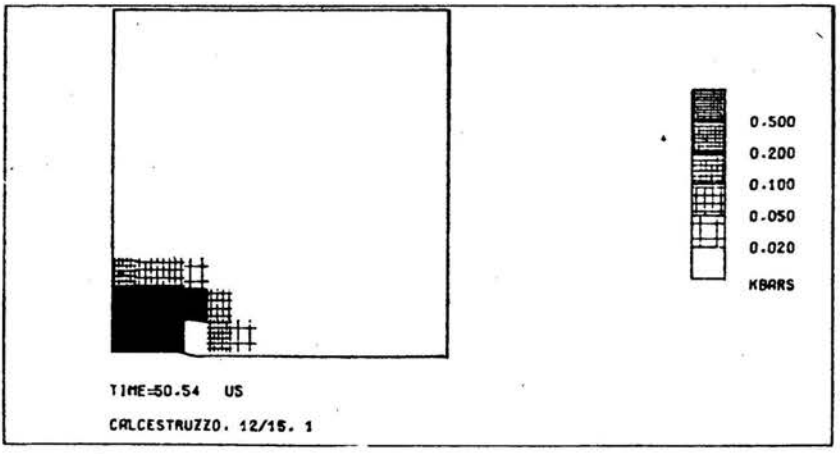

FIG. 18.

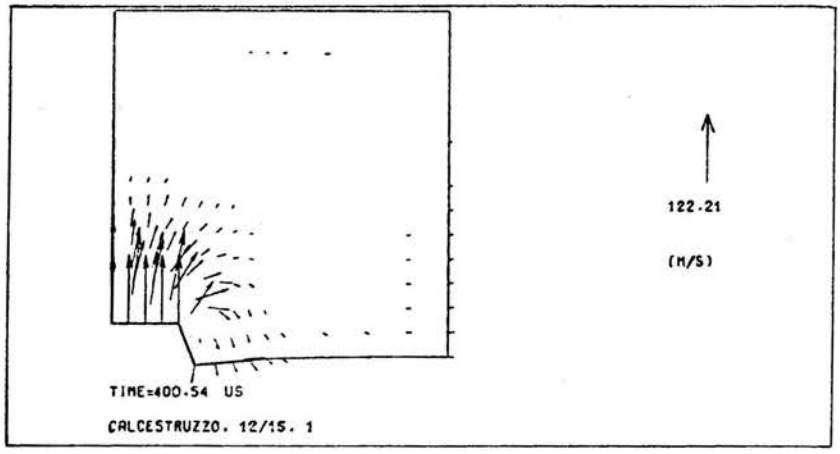

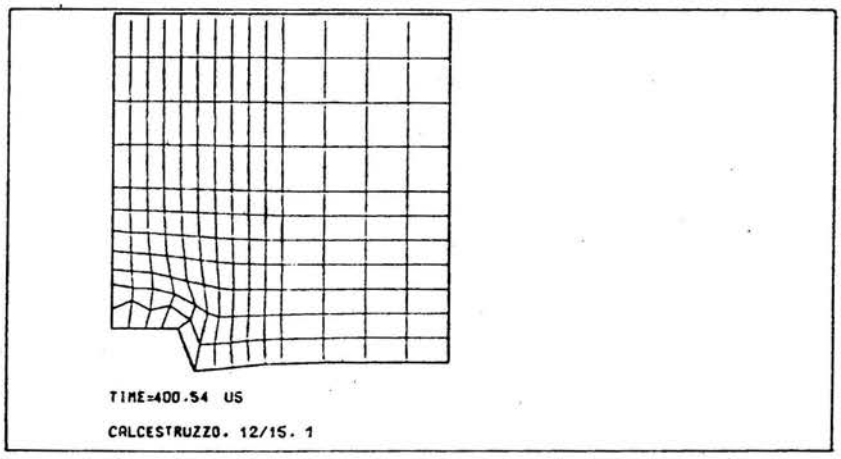

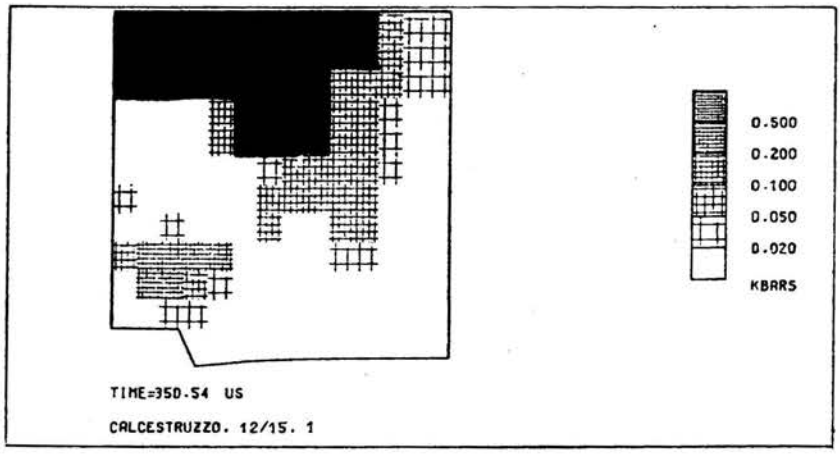

FIG. 19.

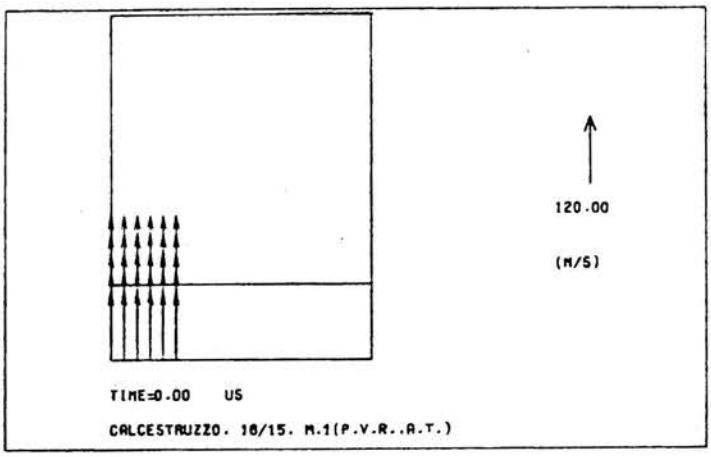

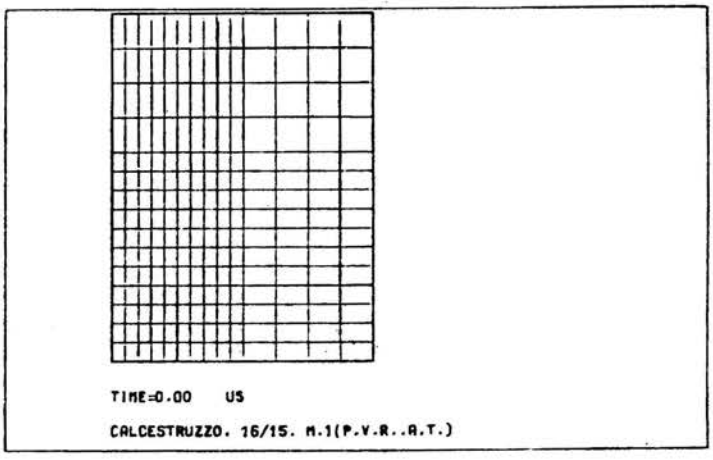

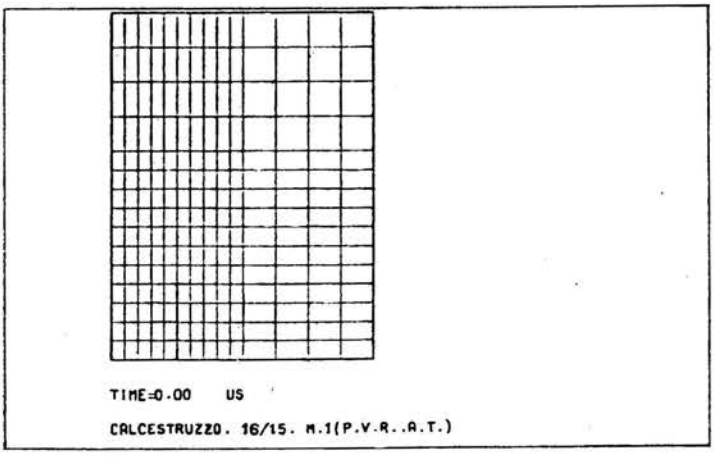

FIG. 20.

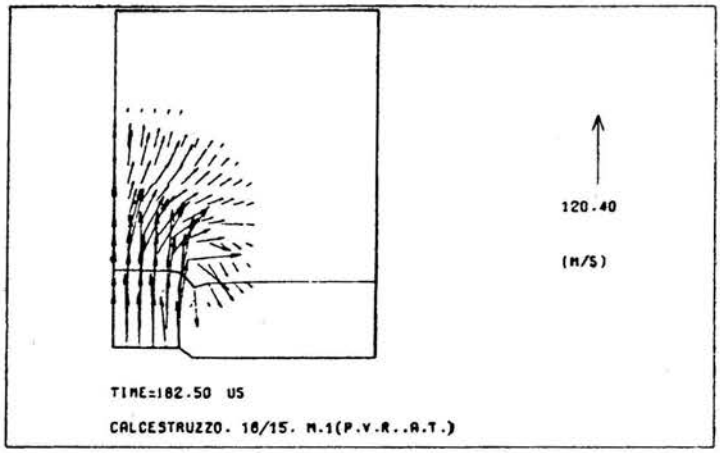

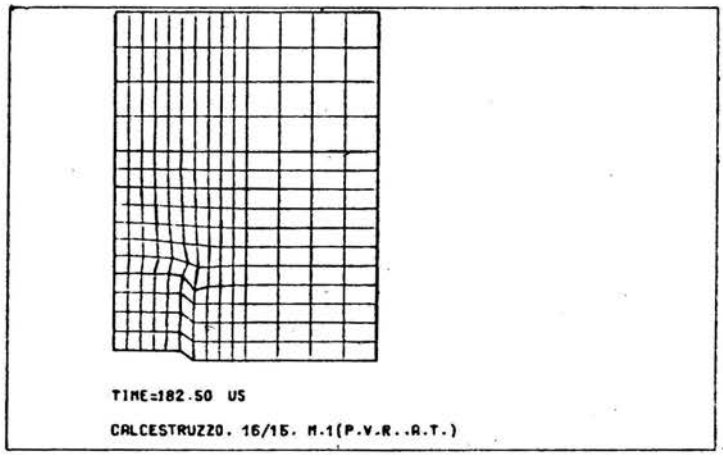

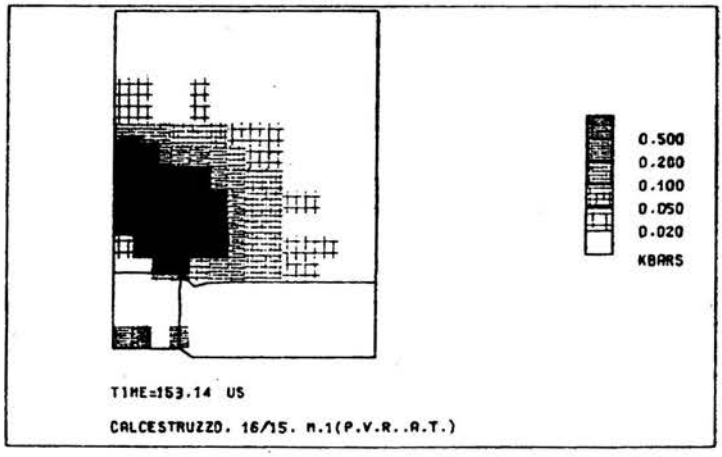

FIG. 21.

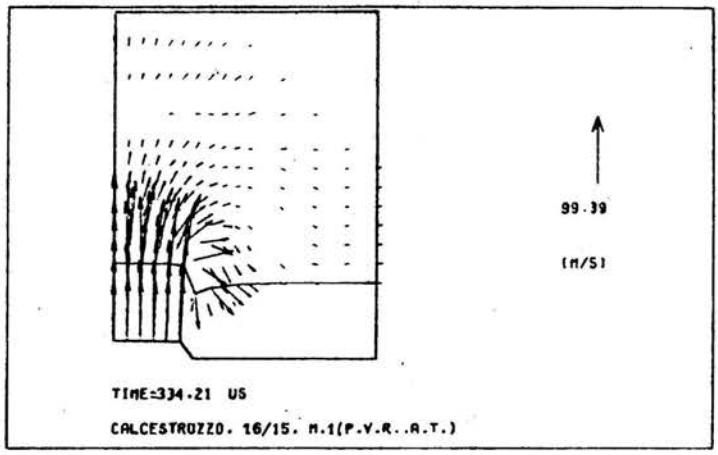

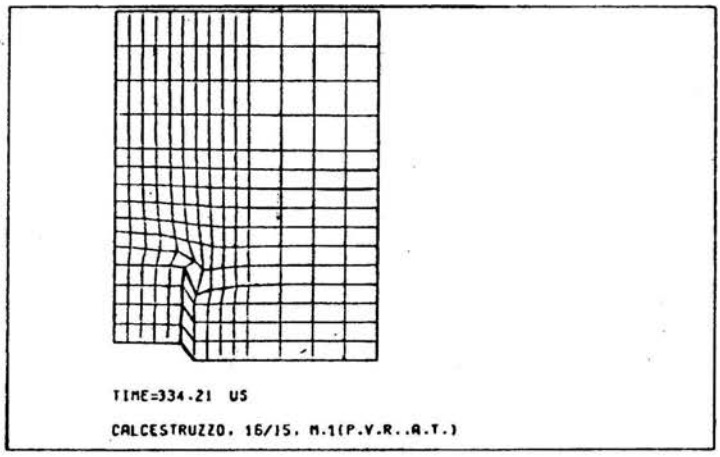

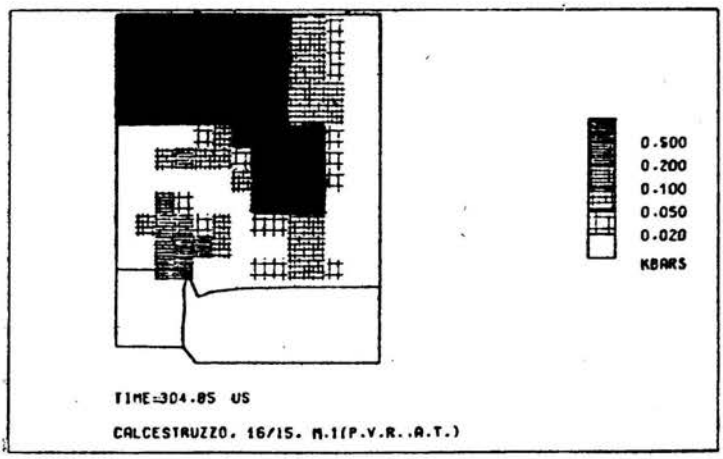

FIG. 22.

the missile penetration and the shock waves 100 μs after impact. Figure 19 is referred at a time of 400μs.

In calculation no 2 (Fig. 20) the steel missile is supposed to have a velocity of 120 m/s. Figures 21 and 22 show the concrete particles' velocity, the concrete network deformation and the shock waves propagation 182 μs and 304 μs after the impact.

From these evaluations one can see a lateral and bottom swelling of the concrete; 600 μs after the impact the bottom surface of concrete is lowered by 4 cm.

6. Influence of stainless steel properties on fast reactor vessel response to an overall core accident

As an example of influence of stainless steel properties on fast reactor containment, a set of calculations have been performed on 1:6 PEC reactor mock-ups designed for explosive tests.

Special care was devoted to analyse the influence of structural material properties on vessel deformations caused by an accidental energy liberation due to an overall core accident.

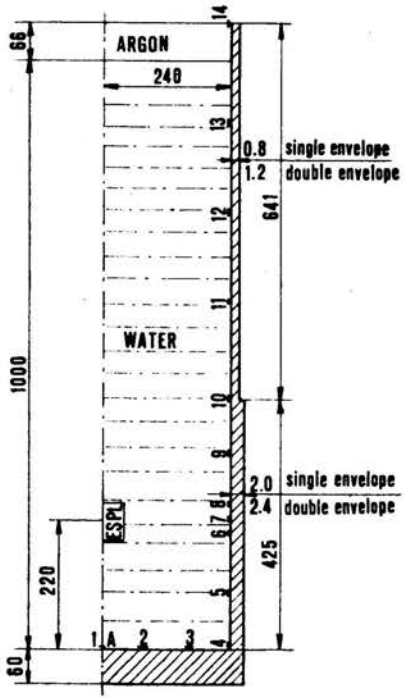

FIG. 23. Computational scheme for the 1:6 PEC reactor mock-up.

Figure 23 shows the computational scheme for the 1:6 scaled PEC reactor mock-up.

Comparison between pressures, impulses and strains in the mock-up have been performed after an energy release inside the reactor vessel corresponding to 200 M Joule in prototype scale.

The computations have been done partly for a single envelope (0.8 and 2.0 cm thick in the upper and lower regions respectively) and partly for a double envelope which has been treated as a single shell (1.2 and 2.4 cm thick respectively).

The source data for the AISI 304 L and 316 L are a set of experimental $\sigma-\varepsilon$ relations referred to various T and $\dot{\varepsilon}$ conditions, reported in Table 1.

Table 1. Temperatures and strain-rates for experimental σ-ε relations.

AISI 304L		AISI 316L	
$T = 20°C$	$T = 550°C$	$T = 20°C$	$T = 400°C$
$10^{-4}s^{-1}$			
10^{-2}	$10^{-2}s^{-1}$	$0.4 \cdot 10^{-2}s^{-1}$	$0.3 \cdot 10^{-2}s^{-1}$
50	126	15	45
110	295	44	70
502	671	420	470

Table 2. Material properties used in the computations.

Cond	Material	Character-istic	Temp. °C	σ_y $\times 10^9$ dyne/cm^2	ε_y	Tangent modulus $\times 10$ dyne/cm^2
2	304 L	dynamic	20	5.4	·0028	8.15
3	304 L	dynamic	550	4.1	·0026	3.40
1	304 L	static	20	4.0	·0021	10.1
4	316 L	static	20	3.5	·0018	12.1
6	316 L	static	400	2.9	·0018	9.10
5	316 L	dynamic	20	5.8	·0030	9.5
7	316 L	dynamic	400	3.9	·0024	5.7

Due to code limitations (REXCO) each experimental $\sigma-\varepsilon$ curve was replaced by two straight segments representing an elastic and a plastic region. This reduces the number of free parameters. The first segment practically coincides with the well-defined linear part of the experimental curve.

The second segment has been defined as imposing area conservation under the $\sigma-\varepsilon$ curve up to $\varepsilon = 0.15$, a strain value which was not exceeded in the computations. The resulting material properties are shown in Table 2 for the minimum and maximum strain rates, here denoted by "static" and "dynamic" characteristics.

Other parameters influencing the material strength are irradiation and manufacturing. Typical experimental indications for an integrated flux of about 10^{20} neutr/cm^2 (neutron energy $E_n > 0.1$ Mev at temperature $400 \div 450°C$) give a $\sim 10\%$ increase in yield and ultimate strength.

For the sake of illustration we shall mainly comment on the principal results referring to the 304 L, dynamic, 20°C case (condition 2 in Table 2).

7. Computational results

7.1. Maximum radial deformation

For all conditions radial deformation is maximum at the charge level or slightly below it. Above this level the deformation first decreases, then increases again due to the wall thickness reduction. Figure 24 shows the double envelope ASTARTE radial deformation as a function of height at three different times for conditions 2 and 5 in Table 2. The deformation is seen not to increase after 400 μs in the thicker lower part of the vessel, while in the proximity and above the change in thickness, the deformation increase continues

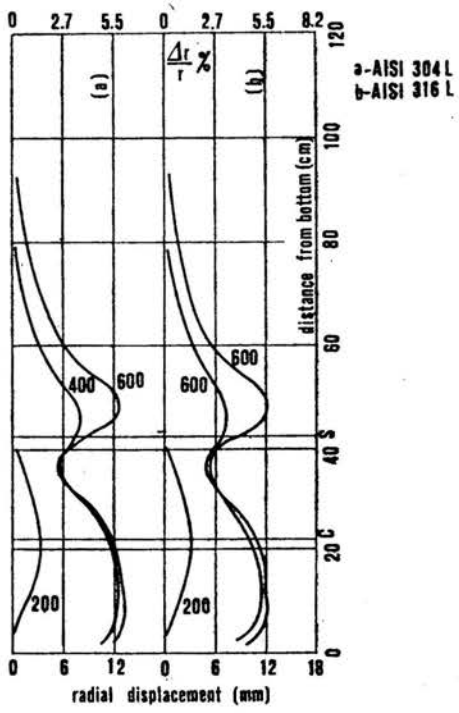

FIG. 24. Deformed wall profiles (time in μs, ASTARTE), *a* — condition 2, Table 2, *b*-condition 5, Table 2.

after 400 μs, reaching about the same (maximum) value as in the lower part. At the time of 600 μs no deformation has yet been detected in the vessel near the plug.

For condition 2 in Table 2, Fig. 3 shows again double envelope ASTARTE deformation as a function of profile height at a fixed time, 600 s, compared with the corresponding REXCO deformation.

The agreement is generally fairly good, though slightly greater deformations are obtained with ASTARTE. In the same condition the maximum deformations as a function of time are reported in Fig. 26 a,b. The corresponding single envelope REXCO maximum deformation is shown in Fig. 26 c. For all times ASTARTE deformations are larger than REXCO's according to Fig. 25. As expected, the single envelope deformations are higher than the double envelope ones.

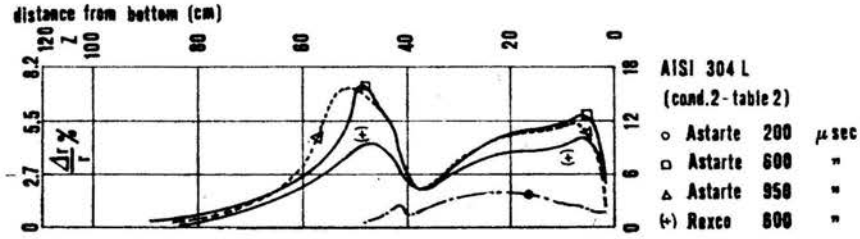

FIG. 25. Deformed wall profiles with membrane theory.

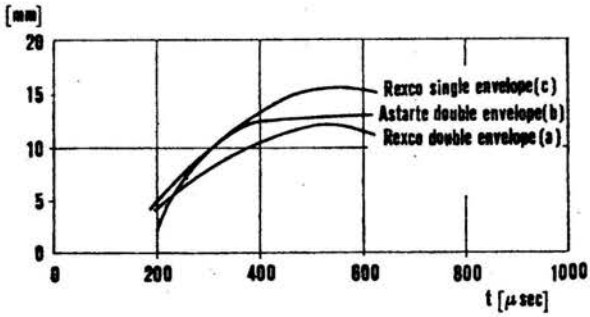

FIG. 26. Maximum deformation as a function of time.

7.2. Effect of material properties

ASTARTE-pressure and impulse values corresponding to the various conditions listed in Table 2 are reported in Table 3 (position numbers refer to Fig. 23).

The first peak (pressure and time) values are practically not influenced by the above conditions, as should be expected. The influence of the conditions listed in Table 2 becomes effective for the second peak values at a greater distance from the charge or, equivalently, at larger times. This should be expected since at such times deformations have occured, the more significant the less the material strength.

For the two materials, AISI 304 L and AISI 316 L, with dynamic $\sigma-\varepsilon$ curves at 20°C, the deformed wall profiles are reported in Fig. 24 a,b at times 200, 400, 600 μs.

7.3. Strain rate computation and influence of the yield stress

The strain rate as a function of time at position B is shown in Fig. 27. From this the dynamic curve used as input receives a substantial aposteriori justification. However, results obtained from $\sigma-\varepsilon$ curves pertaining to different strain rates are nevertheless indicative of how variations of the $\sigma-\varepsilon$ relation can influence the containment response.

The influence of the yield stress on the maximum wall deformation ΔR has also been studied.

Figure 28 reports the results of computation made on the prototype scale with a Belgonucleaire charge of 200 MJ.

Table 3. Peak pressure and arrival time (ASTARTE)

		Position 1 = *A*		Position 2		Position 5		Position 7 = *B*		Position 10		Position 12		
		I peak	II peak	I peak	II peak	I peak	II peak	I peak	II peak	I peak	II peak	I peak	II peak	
304 L	Static 20°C	3.46	3.04	3.06	1.33	1.30	1.47	3.30	0.30	1.84	0.22	0.34	0.21	
		150	300	150	300	150	250	150	300	200	400	350	550	(+)
	Dynamic 20°C	3.49	3.09	3.06	1.44	1.27	1.55	3.33	0.39	1.85	0.47	0.36	0.46	
		150	300	150	300	150	250	1.50	300	200	300	400	500	(+)
	Dynamic 550°C	3.49	3.22	3.06	1.34	1.27	1.47	3.33	0.31	1.85	0.23	0.29	0.20	
		150	300	150	300	150	250	150	300	200	300	400	500	(+)
316 L	Static 20°C	3.48	3.05	3.06	1.38	1.27	1.42	3.33	0.25	1.84	0.30	0.31	0.21	
		150	300	150	300	150	250	150	300	200	400	400	500	(+)
	Dynamic 20°C	3.47	3.10	3.06	1.46	1.29	1.58	3.32	0.41	1.85	0.49	0.36	0.50	
		150	300	150	300	150	250	150	300	200	300	400	500	(+)
	Static 400°C	3.49	2.94	3.06	1.10	1.27	1.42	3.33	0.28	1.82	0.29	0.29	0.22	
		150	300	150	300	150	250	150	300	200	350	400	550	(+)

(+) arrival time of the pressure peak (μsec); pressure in Kbars

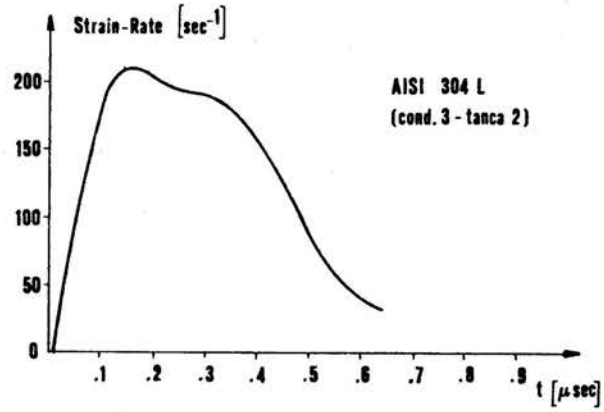

FIG. 27. Strain rate as a function of time.

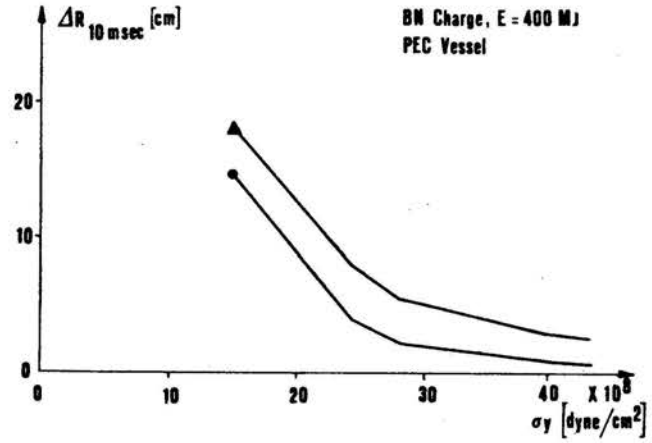

FIG. 28. Radial deformation on prototype vessel.

The $\sigma-\varepsilon$ diagrams used have variable σ_y and a constant tangent modulus E_p. The energy absorbed by the wall is approximately proportional to $\Delta R\sigma_y$ since the elastic limit deformation is very much smaller than $\Delta R/R$, and $E_p(\Delta R/R) \ll \sigma_y$. This energy is seen to decrease with increasing σ_y in Fig. 28.

Conclusion

The safety analysis of nuclear power plants requires the determination of the dynamic response of different containment structures to accidental loadings.

Such an analysis can be performed according to the following steps:

Measurements of stress-strain relations for structural materials (mainly steels and concrete) under monoaxial and pluriaxial dynamic loading. The influence of various parameters (radiation, welding, temperature, strain rate, etc.) must be assessed. Up to now

main efforts in different laboratories have been devoted to monoaxial tests on metallic materials. Current procedures for reinforced concrete structures make use of static test results, but the degree of validity of such assumptions for dynamically-loaded structures has yet to be verified experimentally.

Stress-strain relations have then to be utilized to calibrate the constitutive equations of structural materials including rate sensitivity effects. Different equations of state have been proposed for metallic materials exhibiting strain rate sensitivity, mainly with monoaxial loading. In our future program we foresee to apply our experimental results to such constitutive relations. Failure criteria for concrete under dynamic loadings are pooryl known but the formulation of such laws is essential for use in the design of concrete components.

The response of containment components dynamic loadings requires the finite element method in linear and nonlinear analysis. The available finite element structural codes (like BERSAFE, ADINA, NON-SAP, PISCES, ASTARTE, REXCO) need as input the constitutive laws of materials i.e.: the yield and failure functions and the plastic flow rules including the matrix constitutive relationships in multiaxial loadings. Up to now the material laws inserted in structural codes have not usually taken into consideration strain rate effects which in nuclear accidents may be very important due to highly dynamic loads that are produced and that can affect substantially the response of nuclear plants' structures.

References

1. C. BERIAND *et al.*, N.E.D., **45**, 1978.
2. L. D. BERTHOLF and C. G. KARNES, J. Mech. Phys. Solids, **23**, 1975.
3. U. S. LINDHOLM and L. M. YEAKLEY, Exp. Mech., January 1968.
4. J. L. RAND, U.S. Naval Ordonance Laboratory Report, NOLTR 67, 156, 1967.
5. T. HAYASHI and N. TANIMOTO, IUTAM, Symposium on High Velocity Deformation of Solids, Tokyo 1977.
6. U. S. LINDHOLM and L. M. YEAKLEY, Exp. Mech., January 1967.

J.R.C., ISPRA ESTABLISHMENT, ISPRA

and

UNIVERSITY OF BOLOGNA, ITALY.

Received August 18, 1979.